Two-dimensional kinetics of binary nucleation in sulfuric acid–water mixtures

Robert McGraw
Environmental Chemistry Division, Brookhaven National Laboratory, Upton New York 11973

(Received 30 September 1994; accepted 25 October 1994)

Homogeneous nucleation theory for binary mixtures is developed as a two-component extension of the classical multistate kinetics rate theory. A matrix formulation, based on the stochastic model of Shugard and Reiss [J. Chem. Phys. **65**, 2827 (1976)], provides the framework for solving the strongly coupled two-dimensional flux network associated with tracking the evaporation and growth kinetics of each component for several thousand binary clusters, of varying composition, throughout the region of critical size. This approach avoids the assumption of a single nucleation path, e.g., through the saddle point of the binary free-energy surface, and considers, instead, all possible paths whose current density contributes to the nucleation rate. Calculations are presented for the steady-state nucleation rate and, by a new method based on the negative eigenvalue theorem, for the distribution of relaxation times in sulfuric acid–water mixtures. At water relative humidities typical of the atmosphere, quantitative agreement with the predictions of a closed-form rate expression due to Shugard *et al.* is found. At high supersaturations, typical of diffusion cloud chamber operation, the nucleation current is found to bypass the saddle point, due to kinetic forcing, resulting in a higher-than-expected nucleation rate.

I. INTRODUCTION

Binary homogeneous nucleation is a mechanism for gas-to-particle conversion that can result in significant rates of new particle formation even if both components are undersaturated in the gas phase. An important example is the atmospheric production of sulfuric acid in the presence of ambient water vapor, which has been indicated as a leading mechanism for new particle formation in marine aerosols[1,2] and Arctic haze.[3] New particle formation in the atmosphere inevitably occurs in the presence of background aerosol, in competition with particle growth, and is most prominent in clean environments where the surface area of background aerosol is low. The outcome of the competition between new particle formation and growth, which determines particle size and number density, depends critically on time-dependent nucleation kinetics and on the balance of fluxes at steady state.

From the standpoint of the foundations of classical nucleation theory,[4] binary and single-component nucleation processes have strong similarities: The description of each begins with the capillarity approximation,[4] to obtain the cluster free-energy surface, and detailed balance, to obtain the cluster evaporation rate. Nevertheless, full implementation of the classical theory, which inherently requires a two-dimensional flux network for binary mixtures, to represent the evaporation and growth of each component species, remains incomplete. Previous treatments of binary systems have invoked a reduced-dimensionality assumption by assigning a specific path, generally through the saddle point of the cluster free-energy surface (Sec. IV), along which nucleation is constrained to take place. Limitations of the saddle path assumption, including the possibility that the binary nucleation current can be shifted from the saddle point, where the thermodynamic free energy is lowest, were pointed out by Stauffer,[5] even prior to development of a fully two-dimensional kinetic theory.

The present work was motivated in part by analogy with recent molecular-based treatments of single-component nucleation.[6,7] In the molecular approach, a two-dimensional free-energy surface is introduced (even for a one-component system) and the nucleation rate is given as a sum of contributions from all possible paths over this surface. For binary systems, a two-dimensional surface results even when the treatment remains classical (as in the present paper) and is not molecular based. Conversely, the computational techniques introduced in the present paper may be expected to contribute to further developments of the molecular-based theory.

The matrix formulation of Shugard and Reiss[8] is extended in Sec. II to obtain a fully two-dimensional (2D) description of binary nucleation kinetics. General solutions for the steady-state flux distribution and nucleation rate are obtained. In addition, the matrix formulation is shown to provide a complete description for time-dependent behavior during the approach to steady state. The extended treatment provides a powerful framework for solving the strongly coupled two-dimensional flux network problem associated with tracking the evaporation and growth kinetics for several thousand binary clusters, of varying composition, throughout the region of critical size. The new approach avoids the reduced dimensionality assumption of a single nucleation path, e.g., through the saddle point of the binary free-energy surface, and considers, instead, all possible paths whose current density contributes to the nucleation rate.

The two-dimensional flux network for binary nucleation in sulfuric acid–water mixtures (including hydrates) is constructed in Sec. III. The sulfuric acid–water system was selected both for its importance to atmospheric particle formation[1–3] and because of the existence of a number of well-documented prior studies to which the present results

Downloaded 14 Mar 2005 to 130.199.3.2. Redistribution subject to AIP license or copyright, see http://jcp.aip.org/jcp/copyright.jsp

can be quantitatively compared. Calculations are described in Sec. IV. Steady-state flux distributions and nucleation rates are obtained for both undersaturated, 50% relative humidity (RH), and highly supersaturated (200% and 300% RH) water vapor conditions. The latter conditions, while not observed in the atmosphere, are typical of diffusion cloud chamber operation.[9] The steady-state nucleation rates are compared with those obtained using the model of Shugard *et al.*[10] and suggest a quantitative range of validity to this model that could not have been demonstrated prior to a full 2D analysis of flux contributions to the nucleation rate. The agreement is quantitative except at the highest water supersaturation conditions, typical of diffusion cloud chamber operation, where the saddle path flux model underestimates the nucleation rate. Hydrates are included in the kinetics, following the prescription of Heist and Reiss[11] as described in Ref. 12. Computer codes of Schelling and Reiss[12] were used to obtain the free-energy surface. Results obtained at the highest water supersaturation examined, 300% RH, illustrate a case where steady-state currents are sufficiently controlled by kinetics that the dominant nucleation flux completely bypasses the saddle point.

A new computational approach to time-dependent nucleation, based on the negative eigenvalue theorem,[13] is also presented in Sec. IV. A convenient version of the algorithm, suitable for direct application to compactly stored banded matrices, is described in the Appendix. Since the negative eigenvalue theorem can be used to rapidly locate each eigenvalue (relaxation time) of the rate matrix, it represents a significant advance over variational methods, which have been limited in application to determination of an upper bound for the smallest eigenvalue or, equivalently, a lower bound for the longest relaxation time, or lag time, governing the approach to steady state. The method is used to obtain cumulative relaxation time distributions for the description of nonsteady-state behavior in sulfuric acid–water mixtures. Section V presents a discussion and summary of results.

While this paper was in its final stages of preparation, the author received a preprint[14] that uses a similar matrix method to obtain the steady-state flux distribution in two dimensions. Calculations for the steady-state nucleation rate were carried out for sulfuric acid–water mixtures (30%–90% RH), and for the ammonia–water system. Order-of-magnitude agreement between the rates predicted by the matrix method and by the Stauffer theory[5] were found for the sulfuric acid–water mixtures. The present study differs from Ref. 14 in its inclusion of hydrates, comparisons with the binary theory of Ref. 10, and extension of the matrix method to the time-dependent domain for calculation of the relaxation time distribution.

II. MATRIX FORMULATION

Figure 1 shows the basic configuration for fluxes to and from a binary cluster of size (i,j) containing i molecules of component 1 and j molecules of component 2. The equation for the net current for conversion of clusters of size (i,j) to size $(i+l,j)$ takes the form

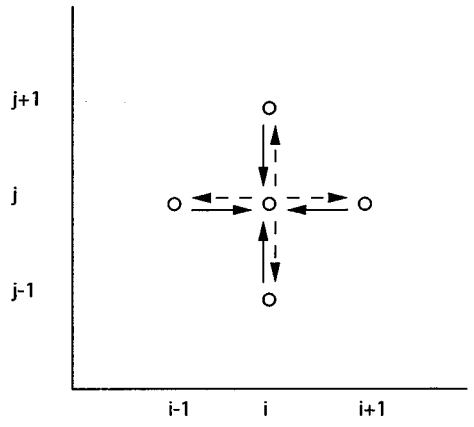

FIG. 1. Fluxes for cluster evaporation and growth. Solid (dashed) arrows show the positive (negative) contribution to the time evolution of clusters of size (i,j).

$$J_1(i,j)=\beta_1 s(i,j)f(i,j)-\gamma_1(i+1,j)s(i+1,j)f(i+1,j), \tag{2.1a}$$

where the subscript 1 refers to the i coordinate (horizontal flux) from cluster (i,j). Similarly, for the net current for conversion of clusters of size (i,j) to size $(i,j+1)$:

$$J_2(i,j)=\beta_2 s(i,j)f(i,j)-\gamma_2(i,j+1)s(i,j+1)f(i,j+1), \tag{2.1b}$$

where the subscript 2 refers to the j coordinate (vertical flux) from cluster (i,j). In these equations, $\beta_1(\beta_2)$ is the accommodation rate per unit area of surface for molecules of component 1 (component 2), $s(i,j)$ is the surface area, and $f(i,j)$ is the concentration of clusters of size (i,j).

At equilibrium the net flux vanishes and

$$\beta_1 s(i,j)n(i,j)=\gamma_1(i+1,j)s(i+1,j)n(i+1,j), \tag{2.2}$$

where $n(i,j)$ is the cluster concentration at equilibrium. This expression of principal of detailed balance is used to eliminate the size-dependent cluster evaporation rate γ_1. A similar equation is formed from the right-hand side of Eq. (2.1b) for elimination of γ_2. Then the equations for the net currents take the form

$$J_1(i,j)=\beta_1 s(i,j)n(i,j)\left[\frac{f(i,j)}{n(i,j)}-\frac{f(i+1,j)}{n(i+1,j)}\right] \tag{2.3a}$$

and

$$J_2(i,j)=\beta_2 s(i,j)n(i,j)\left[\frac{f(i,j)}{n(i,j)}-\frac{f(i,j+1)}{n(i,j+1)}\right]. \tag{2.3b}$$

Time evolution of the cluster population is given in terms of the currents specified by Eqs. (2.3):

$$\frac{df(i,j)}{dt}=J_1(i-1,j)-J_1(i,j)+J_2(i,j-1)-J_2(i,j) \tag{2.4}$$

together with the boundary conditions for monomer,[4] e.g., $f(1,0)/n(1,0)=1$, and the Szilard boundary conditions $f(i,j)=0$ along a specified outer path having sufficiently

Downloaded¬14¬Mar¬2005¬to¬130.199.3.2.¬Redistribution¬subject¬to¬AIP¬license¬or¬copyright,¬see¬http://jcp.aip.org/jcp/copyright.jsp

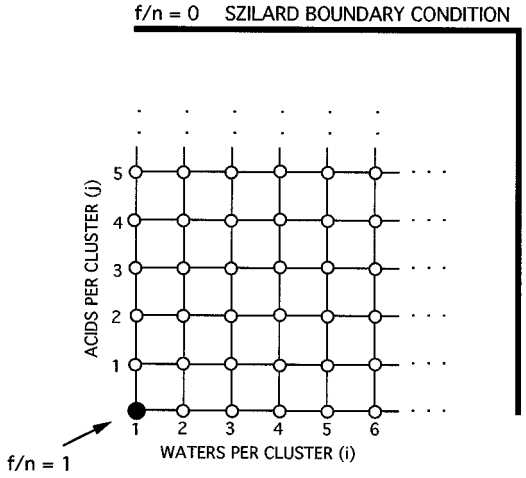

FIG. 2. Two-dimensional network configuration for describing binary nucleation kinetics in sulfuric acid–water mixtures. Each open circle node corresponds to an (i,j) cluster whose concentration is to be determined and contributes to the dimensionality of **f**. The figure also shows the free water monomer and Szilard boundary conditions.

large values of i and j (Fig. 2). As in the case of one-component systems, the Szilard boundary should be sufficiently removed from the critical cluster size (saddle point location) that the steady-state currents and steady-state concentrations are insensitive to its position. Equations (2.3) and (2.4) can be combined to express the evolution of the cluster population in vector–matrix form:

$$\frac{d\mathbf{f}}{dt}=\mathbf{K}\mathbf{f}+\mathbf{a}, \tag{2.5}$$

where **f** is the cluster population vector and the **a** is a constant vector dependent on source rates at the monomer boundary condition.

Equations (2.3), extended over a range of cluster size, describe a system similar to an electrical network with the various f/n as potentials and J as currents. This analogy is explored further in Sec. IV C below. The quantities $\beta_{1,2}$ and s are known, or can be estimated, from the physical properties of the system, and the equilibrium concentrations $n(i,j)$ are obtained in the usual manner from the free-energy surface, which is itself derived using the capillarity approximation.[4] This system of equations can be solved for the concentrations $f(i,j)$, once the boundary conditions on the potentials f/n have been specified. When these concentrations are substituted back into Eqs. (2.3) the horizontal and vertical currents are obtained.

The elements of the matrix **K** are determined from Eqs. (2.3) and (2.4) following the positioning of the elements of **f**. A straightforward way to proceed is to set up a one-to-one mapping $k\leftrightarrow(i,j)$, $l\leftrightarrow(i',j')$ between the components of **f** and the cluster composition (i,j). The specific mapping depends on the monomer boundary condition as shown below in Sec. III. Then the five classes of nonzero entries to consider with nearest-neighbor transformations (Fig. 1) are listed in Table I and result in a nonsymmetric banded structure for the matrix **K**.

TABLE I. Scheme for assigning the nonzero elements of **K**.

$K_{kl}=\beta_1 s(i,j)\dfrac{n(i,j)}{n(i+1,j)}$	for $k\leftrightarrow(i,j)$ and $l\leftrightarrow(i+1,j)$
$K_{kl}=\beta_2 s(i,j)\dfrac{n(i,j)}{n(i,j+1)}$	for $k\leftrightarrow(i,j)$ and $l\leftrightarrow(i,j+1)$
$K_{kl}=\beta_1 s(i-1,j)$	for $k\leftrightarrow(i,j)$ and $l\leftrightarrow(i-1,j)$
$K_{kl}=\beta_2 s(i,j-1)$	for $k\leftrightarrow(i,j)$ and $l\leftrightarrow(i,j-1)$
$K_{kk}=-\left[\beta_1 s(i-1,j)\dfrac{n(i-1,j)}{n(i,j)}+\beta_1 s(i,j)\right]-\left[\beta_2 s(i,j-1)\dfrac{n(i,j-1)}{n(i,j)}+\beta_2 s(i,j)\right]$	for the main diagonal $k\leftrightarrow(i,j)$

Each of the eight terms in Table I corresponds to a vector in Fig. 1. Four of these terms, corresponding to the dashed vectors in Fig. 1, appear in the diagonal element K_{kk} and make a negative (loss) contribution to the right-hand side of Eq. (2.4). Certain properties of the elements of **K** are evident from Table I: For each element k connected in reciprocal fashion to its neighbors (i.e., not next to the monomer or Szilard boundary locations) the sum of the elements in column k of **K** equals zero. An important additional property, relating K_{kl} and K_{lk} through detailed balance, is given by Eq. (2.12) below. From Eqs. (2.3) and Table I it is seen that the net current for transformation of clusters of type $k\leftrightarrow(i,j)$ to type $l\leftrightarrow(i',j')$ can be written in the form

$$J(k\rightarrow l)=K_{lk}f_k-K_{kl}f_l \tag{2.6}$$

which vanishes when the equilibrium cluster concentrations $n(i,j)$ are substituted for $f(i,j)$. Finally, it should be noted that transformations beyond nearest neighbors, if required, are accommodated within the matrix formulation simply by adding more nonzero elements to **K**. In Sec. III it will be shown that nearest-neighbor transformation is sufficient for describing nucleation in sulfuric acid–water mixtures, even when collisions with hydrate clusters are included in the model.

A. Steady-state solution

The steady-state solution to Eq. (2.5) is obtained through matrix inversion as follows: First, separate **f** into its transient and steady-state components. Following the notation of Schelling and Reiss[12]:

$$\mathbf{f}=\mathbf{g_T}+\mathbf{g_{SS}}. \tag{2.7}$$

Substitution into Eq. (2.5) gives

$$\frac{d\mathbf{g_T}}{dt}=\mathbf{a}+\mathbf{K}\mathbf{g_{SS}}+\mathbf{K}\mathbf{g_T}. \tag{2.8}$$

The requirement that the transient solution decay to zero at long time implies that $\mathbf{a}+\mathbf{K}\mathbf{g_{SS}}=\mathbf{0}$ or, equivalently,

$$\mathbf{g_{SS}}=-\mathbf{K}^{-1}\mathbf{a}. \tag{2.9}$$

Downloaded 14 Mar 2005 to 130.199.3.2. Redistribution subject to AIP license or copyright, see http://jcp.aip.org/jcp/copyright.jsp

Obtaining the steady-state network solution is, therefore, equivalent to finding the inverse of the matrix **K**.

B. Transient solution

Substitution of Eq. (2.9) into Eq. (2.8) gives the fundamental equation for the transient component of **f**:

$$\frac{d\mathbf{g_T}}{dt}=\mathbf{K}\mathbf{g_T}. \tag{2.10}$$

To proceed further it is useful to convert the rate matrix to Hermitian form. For a one-dimensional nucleation path, the matrix **K** is tridiagonal and readily converted to Hermitian form by similarity transformation using diagonal matrices.[8] However, the approach developed in Ref. 8 is not inherently limited to 1D systems and it is easy to show that the same similarity transformation also converts a nontridiagonal **K**, arising from the 2D flux problem, to Hermitian form. This is shown as follows.

Define the diagonal matrix:

$$D_{kk}=\exp[w(i,j)/kT] \tag{2.11}$$

whose elements correspond to the $k\leftrightarrow(i,j)$ mapping. $w(i,j)\equiv w_k$ is the free energy for forming a cluster of type (i,j). Since the equilibrium concentrations $n(i,j)$ are themselves proportional to the Boltzmann factors $\exp[-w(i,j)/kT]$, inspection of Table I reveals that for all pairs (k,l), the following identity holds:

$$K_{lk}=\exp[(w_k-w_l)/kT]K_{kl}. \tag{2.12}$$

Equation (2.12) has its origin in the detailed balance condition. Note that when Eq. (2.12) is substituted into the current formula [Eq. (2.6)] for $J=0$, the equilibrium population distribution is obtained. From Eqs. (2.11) and (2.12), the transpose of **K** is

$$\mathbf{K^T}=\mathbf{DKD}^{-1}. \tag{2.13}$$

With **K** and **D**, the Hermitian matrix **H** can be constructed. Consider

$$\mathbf{H}=-\mathbf{D^{1/2}KD^{-1/2}}, \tag{2.14}$$

where $\mathbf{D^{1/2}}$ is the square root of the diagonal matrix **D**. Then

$$\begin{aligned}\mathbf{H^T}&=-(\mathbf{D^{1/2}KD^{-1/2}})^{\mathbf{T}}=-\mathbf{D^{-1/2}K^TD^{1/2}}\\&=-\mathbf{D^{-1/2}DKD^{-1}D^{1/2}}=-\mathbf{D^{1/2}KD^{-1/2}}=\mathbf{H},\end{aligned} \tag{2.15}$$

where Eq. (2.13) has been used. This derivation shows that **H** is brought to Hermitian form by a similarity transformation with a diagonal matrix whose elements are the square root of the Boltzmann factors in terms of which the equilibrium cluster populations are defined. Note that the key step in proving the Hermiticity of **H** lies in demonstrating, through the entries in Table I, that Eq. (2.12) extends to the 2D flux case. This result is used in Eq. (2.13). The remaining steps in the proof are formally identical to the 1D derivation of Ref. 8. Note, finally, that since the transformation matrices are diagonal, **H** has the same banded structure (Sec. IV) as does **K**, but is in symmetric form.

We can now describe the kinetics in the frame of the transformed matrix **H**. Let

$$\psi_{\mathbf{T}}=\mathbf{D^{1/2}g_T} \tag{2.16}$$

then from Eqs. (2.10) and (2.14) we obtain

$$\frac{\mathbf{d}\psi_{\mathbf{T}}}{\mathbf{dt}}=-\mathbf{H}\psi_{\mathbf{T}}. \tag{2.17}$$

The formal solution to Eq. (2.17) is

$$\psi_{\mathbf{T}}(\mathbf{t})=\mathbf{V}\exp(-\mathbf{D}_\lambda\mathbf{t})\mathbf{V^{-1}}\psi_{\mathbf{T}}(\mathbf{0}), \tag{2.18}$$

where **V** diagonalizes **H**:

$$\mathbf{V^{-1}HV}=\mathbf{D}_\lambda \tag{2.19}$$

and $\mathbf{D}_\lambda$ is the resulting diagonal matrix having the eigenvalues of **H** as elements:

$$(D_\lambda)_{ii}=\lambda_i. \tag{2.20}$$

Since the columns of **V** are the eigenvectors of **H**, Eq. (2.18) may be put into more explicit form. In Dirac notation:

$$\psi_{\mathbf{T}}(\mathbf{t})=\sum_{\mathbf{i}}\langle\psi_{\mathbf{T}}(0)|\mathbf{V_i}\rangle\exp(-\lambda_{\mathbf{i}}\mathbf{t})|\mathbf{V_i}\rangle \tag{2.21}$$

showing the full dependence on the eigenvalues $\{\lambda_i\}$ and eigenvectors $\{\mathbf{V_i}\}$ of **H**. The initial condition used in computing the inner products (local density of states) of Eq. (2.21) follows from (Eq. 2.16). For example, if $\mathbf{f}(0)=0$ then $\psi_{\mathbf{T}}(\mathbf{0})=-\mathbf{D^{1/2}g_{SS}}$. Equations (2.7), (2.9), (2.16), and (2.21) provide a complete solution for the time-dependent flux distribution and nucleation rate.

III. TWO-DIMENSIONAL FLUX NETWORK FOR BINARY NUCLEATION IN SULFURIC ACID–WATER MIXTURES

In Sec. II, the matrix formulation was developed in a framework suitable for describing nucleation in general binary mixtures. Here we apply the model specifically to sulfuric acid–water mixtures. To establish the rates of intercluster conversion, which comprise the matrix elements of **K**, it is convenient to make two simplifying approximations for the vapor phase, which will be shown to be well satisfied for the system under study. These approximations are introduced specifically for the purpose of treating hydrate clusters within the framework of the general matrix approach developed in Sec. II, and are not restrictions on that approach. For binary systems where clustering in the vapor phase in unimportant, the general model can be immediately applied.

First, most of the vapor-phase acid molecules are in the form of $(h,1)$-hydrate clusters consisting of h molecules of water (component 1) and a single molecule of acid (component 2). At 298 K, Jaecker-Voirol and Mirabel estimate that at 200% RH, 99.8% of the acids are bound into these hydrates, at 50% RH the percentage is still 98.8%.[9] For setting up the flux network, with appropriate monomer boundary conditions, we will therefore neglect free-acid molecules and acid clusters and consider only monoacid hydrates and free-water molecules in the vapor phase. This is the first approximation.

The second approximation is that sulfuric acid, in any of its hydrate forms, is present in only trace amounts, compared to the amount of water vapor present, since only trace

Downloaded¬14¬Mar¬2005¬to¬130.199.3.2.¬Redistribution¬subject¬to¬AIP¬license¬or¬copyright,¬see¬http://jcp.aip.org/jcp/copyright.jsp

amounts of sulfuric acid are required in the presence of water to obtain high nucleation rates. To see where this approximation enters, we return to the flux description of Fig. 1: Equations (2.1a) give the flux for conversion of clusters of size i,j to clusters of size $i+1,j$ through the addition of water monomer, which is the dominant species. Equations (2.1b) give the conversion of clusters of size i,j to clusters of size $i,j+1$, nominally through the addition of a single molecule of acid. However, as noted above, most acid molecules are bound with water in hydrate form. Since most hydrates contain a single acid, the addition of the hydrate will indeed change the index j of the cluster by unity. However, we still need to examine changes in the index i that occur with hydrate addition. From the preceding discussion it is clear that hydrate additions will appear in Fig. 1 as fluxes with both horizontal and vertical components, depending on the water content of the colliding hydrate species. This apparent difficulty is easily circumvented by invoking the second approximation above, namely, that for all cases of practical interest, water is the greatly dominant species and the number of free-water molecules far exceeds the number of hydrates. Consider, e.g., that the fluxes due to hydrate addition have been resolved into their horizontal (i) and vertical (j) components. Since water collisions dominate, any contribution to the horizontal flux from hydrate collisions will be insignificant compared to the horizontal fluxes due to the condensation and evaporation of water itself. Thus we can neglect the horizontal component of the fluxes due to hydrate addition. The vertical fluxes, on the other hand, result largely from the addition of monoacid hydrates, which change the cluster index j by unity. These are included in Eq. (2.1b).

To incorporate hydrates in the elements of **K**, the product $\beta_2 s(i,j)$ is replaced by an average over hydrate species and is identical to the quantity $\nu(i,j)$ defined in Ref. 12:

$$\beta_2 s(i,j)=(8\pi kT)^{1/2}\sum_h \sigma_h^2 \mu_h^{-1/2} n(h,1). \tag{3.1}$$

In this equation, σ_h is the sum of the radii of the colliding species, μ_h is the corresponding reduced mass, and $n(h,1)$ is the equilibrium number density of hydrates containing h water molecules. The accommodation rate of the remaining vapor species, single water molecules, on a cluster of surface area $s(i,j)$ is given in the usual manner:

$$\beta_1 s(i,j)=\left(\frac{kT}{2\pi m_1}\right)^{1/2} s(i,j)n(1,0), \tag{3.2}$$

where m_1 is the water monomer mass and an accomodation coefficient of unity is assumed.

The second approximation, above, is equivalent to the condition.

$$\beta_1 s(i,j) \gg \beta_2 s(i,j). \tag{3.3}$$

Note that if Eq. (3.3) were not satisfied for the hydrate clusters, the general matrix formulation could still be applied, but would require the introduction of non-nearest-neighbor transformations in the flux network of Fig. 2.

In the absence of free acids, the network shown in Fig. 2 results. The small cluster (monomer) boundary conditions are simplified in that water is the only free species whose concentration is explicitly fixed. (The fixed activity of acid is implicit in β_2.) Thus from Eq. (2.3):

$$J_1(1,0)=\beta_1 s(1,0)n(1,0)\left[1-\frac{f(2,0)}{n(2,0)}\right], \tag{3.4a}$$

$$J_2(1,0)=\beta_2 s(1,0)n(1,0)\left[1-\frac{f(1,1)}{n(1,1)}\right], \tag{3.4b}$$

where the monomer boundary condition $f(1,0)/n(1,0)=1$ has been used. Note that the element $f(1,0)$, corresponding to the concentration of water monomer, will not appear in **f** as this is held constant by the boundary condition. Thus the ordering of the elements of **f** begins with (1,1) and is carried out so as to minimize the bandwidth of the **K** matrix. Let the network extend to a maximum of $n1$ max water molecules per cluster and $n2$ max acids. Then **f** will be a vector of length $n1$ max $(n2$ max$+1)-1$ with elements:

$$\mathbf{f}^{\mathbf{T}}=[f(1,1),f(1,2),\ldots,f(1,n2\ \text{max}),f(2,0),\ldots, f(n1\ \text{max},\ n2\ \text{max})], \tag{3.5}$$

where $\mathbf{f}^T$ denotes the transpose of **f**. All but two elements of the constant source vector **a** [Eq. (2.5)] are zero and these nonzero elements are determined from the terms in Eqs. (3.4) corresponding to the flux to (1,1) from hydrate combination with water monomer, and the flux to (2,0) from water–water collisions. Comparison with Eq. (3.5), for the positions of these elements, shows that the nonzero elements of **a** are

$$\mathbf{a}_1=\beta_2 s(1,0)f(1,0),$$
$$\mathbf{a}_{n2\ \text{max}+1}=\beta_1 s(1,0)f(1,0). \tag{3.6}$$

The dimensionality of the square matrix **K** matches the length of the vector **f**. The matrix is five-banded with no nonzero elements at a distance greater than $n2$ max$+1$ from the main diagonal. The network of Fig. 2 determines the one-to-one mapping $k\leftrightarrow(i,j)$ of Sec. II with

$$k=(n2\ \text{max}+1)(i-1)+j. \tag{3.7}$$

IV. CALCULATIONS

All parameters needed for the following calculations, e.g., surface tension of the solution, partial molar volumes, chemical potentials, etc., are as assigned in the computer codes of Schelling and Reiss;[12] except for the equilibrium vapor pressure of pure sulfuric acid for which the more recent measurement of Chu and Morrison is used.[15] This assignment, 3.1×10^{-5} Torr at 298 K, is in the range of the measurements of Ayers *et al.*[16] advocated in Ref. 9. The free-energy surfaces at 50% RH and 200% RH obtained for these parameters are shown in Fig. 3. The corresponding acid activities[11] of 1.0×10^{-3} at 50% RH and 1.2×10^{-6} at 200% RH were selected to yield test conditions similar to those of Ref. 12.

Results of the full 2D nucleation kinetics calculations are presented for the preceding two sets of conditions and also for a 300% RH condition. In the examples treated below, we

Downloaded¬14¬Mar¬2005¬to¬130.199.3.2.¬Redistribution¬subject¬to¬AIP¬license¬or¬copyright,¬see¬http://jcp.aip.org/jcp/copyright.jsp

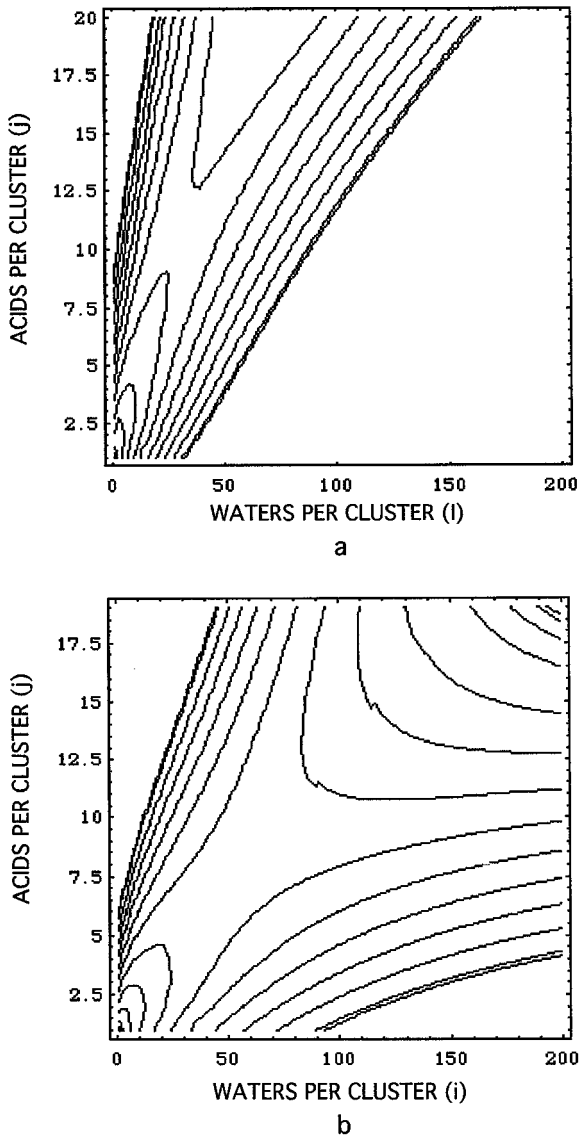

FIG. 3. Free-energy surfaces for sulfuric acid–water clusters in the capillarity approximation. The vertical and horizontal coordinates give the number of acid molecules and water molecules, respectively, in the binary cluster. (Top) water RH=50%; acid activity=$1.0e-03$. (Bottom) water RH =200%; acid activity=$1.2e-06$. Contour spacing=10 kT. Outer contours are more closely spaced for reference at 100 and 102 kT.

consider clusters from 0 to 20 or 25 acids, and from 1 to 200 water molecules in size. This corresponds to a **K**-matrix dimensionality in the 4000 range.

A. Steady-state flux distribution

Solutions for the steady-state cluster population and flux distribution require inversion of the matrix **K** used in Eq. (2.9). Elements of the source vector **a** follow Eq. (3.4) and the monomer boundary condition $f(1,0)/n(1,0)=1$. Because of its large size, and sparse banded structure, **K** is stored in compressed form. Matrix inversion was accomplished using compressed banded matrix subroutines.[17] Calculations were carried out in double precision (19 decimal places). Steady-state fluxes were computed from Eqs. (2.6)

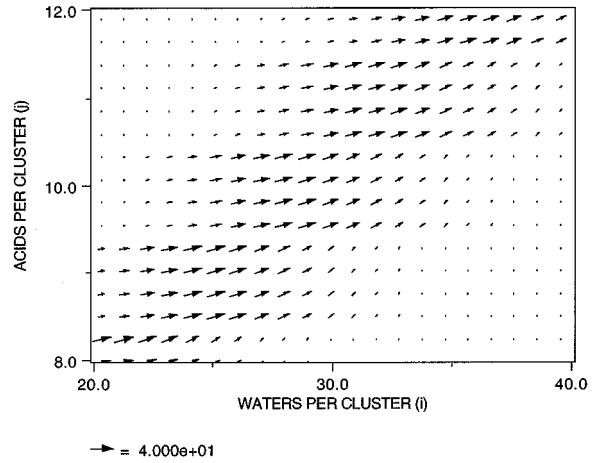

FIG. 4. Steady-state currents in the saddle point region for water RH=50% and acid activity=$1.0e-03$.

upon substitution of the steady-state cluster concentrations obtained from the solution vector $\mathbf{g}_{SS}$. The recovery of **a**, upon multiplication of the solution vector by $-\mathbf{K}$ [Eq. (2.9)], was used as a check on the matrix inversion calculation.

Steady-state currents in the vicinity of the saddle point region are shown in Figs. 4 and 5. Note that, while these currents are defined and computed only for integers i and j, the vector plot routine interpolates for fractional i and j values. Figure 4 (50% RH) shows the flux stream passing through the saddle region and continuing to follow the narrow valley of the free-energy surface. This trend continues, with a slight broadening of the current stream as more acids are added, corresponding to a similar broadening of the free-energy valley, until the horizontal portion of the Szilard boundary (Fig. 2) is reached at the j-range limit of the calculation. At 200% RH the free-energy surface [Fig. 3(b)] acquires a more complex shape. The flux stream, shown in Fig. 5, traverses the saddle region and subsequently proceeds in the direction of water growth. This trend continues until

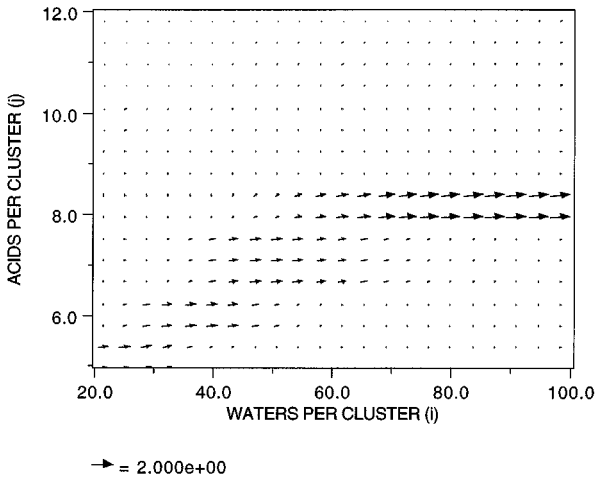

FIG. 5. Steady-state currents in the saddle point region for water RH=200% and acid activity=$1.2e-06$.

Downloaded¬14¬Mar¬2005¬to¬130.199.3.2.¬Redistribution¬subject¬to¬AIP¬license¬or¬copyright,¬see¬http://jcp.aip.org/jcp/copyright.jsp

TABLE II. Results for sulfuric acid–water mixtures. The SHR nucleation rate was computed using Eq. (4.1).

Relative humidity	Acid activity	Nucleation rate (2D) ($cm^{-3}\,s^{-1}$)	Nucleation rate (SHR) ($cm^{-3}\,s^{-1}$)
50%	1.0(−3)	76.91	76.94
200%	1.2(−6)	1.96	1.84
300%	1.0(−8)	2.1(3)	0.5

the vertical portion, i-range limit, of the Szilard boundary shown in Fig. 2 is reached; at which point approximately 93% of the total current is along the $j=8$ path.

The nucleation rate consists of contributions from all possible paths throughout the network and is evaluated as a sum over all currents reaching the Szilard boundary. Table II shows results from the present 2D network calculations for the steady-state nucleation rate together with a comparison with the rate computed using the Shugard–Heist–Reiss SHR model.[10] At 300% RH, more than 99% of the total current is along the $j=2$ path, and continues to follow this path, until the Szilard boundary is reached. (Since a vector plot on the scale of Figs. 4 and 5 indicates only the $j=2$ flux path, no separate figure for this case is shown.) At 300% RH, the saddle point, corresponding to a critical cluster containing 4 acid and 32 water molecules and a barrier height of 49.1 kT, is *not* reached by the current stream. Instead, the predominant nucleation flux is found to skirt over a higher pass in the direction of the water coordinate, which peaks at a cluster size of 2 acid and 106 water molecules and a barrier height of 53.2 kT. Under these conditions the model of Ref. 10, for which the nucleation current is constrained to pass through the saddle point, gives a three order of magnitude underestimate of the nucleation rate. This interesting case confirms the Stauffer prediction,[5] mentioned in Sec. I, and would seem to require a rexamination of the definition of critical cluster size, perhaps to include the kinetic as well as thermodynamic forcing properties of the system. The conventional 1D path approaches, which constrain the flux to pass through the thermodynamic saddle point, may in general be expected to underestimate the nucleation rate by neglecting the more favorable kinetic forcing mechanism. Nonetheless, even at 200% RH, the SHR model underestimates the rate by less than 10%, and a comparison of Figs. 3(b) and 5 shows that most of the current still passes through the saddle region.

Two independent checks were made on the present method of analysis. First, the diagonal elements of **K**, for those nodes adjacent to the Szilard boundary, were each modified to remove the boundary sink term (Table I) and the steady-state solution vector obtained as before. As required for this case, the steady-state currents were found to vanish and the steady-state and equilibrium cluster concentrations were found to be identical. As a second test, β_2 was set equal to zero, forcing the nucleation to occur along the single-component water path. In this case the computed nucleation rate was found to agree with the result obtained independently from the Becker–Doring rate formula for single-component (water) nucleation.[4]

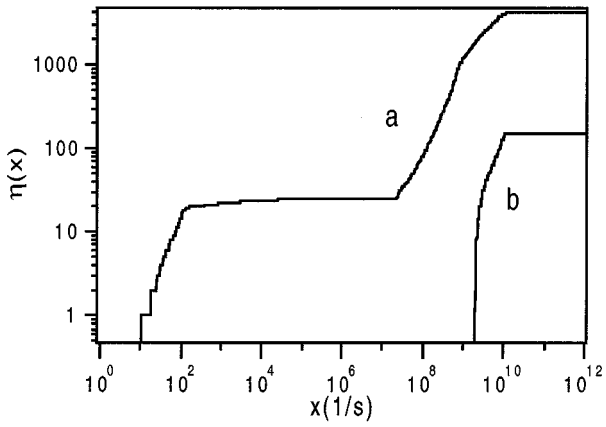

FIG. 6. Cumulative eigenvalue distribution for water RH=50% and acid activity=1.0e−03 (curve a). Plots show $\eta(x)$ for 1000 values of x equally spaced over the logarithmic scale of the figure where $\eta(x)$ gives the number of eigenvalues less than x. Units of x are s^{-1}. Curve b gives the cumulative eigenvalue distribution for pure water at 50% RH, corresponding to relaxation of the water cluster ($j=0$) population.

B. Relaxation time distribution

Equation (2.21) shows that the description of time-dependent nucleation is complete once the solution to the eigensystem associated with the rate matrix **H** has been obtained. However, matrix diagonalization is generally not feasible for application to binary nucleation due to the large matrix size. Here we present a new computational approach to time-dependent nucleation based on the negative eigenvalue theorem (Appendix). The theorem allows the distribution and/or localization of the eigenvalues of **H** to be efficiently determined without diagonalization. Since eigenvalue localization can be carried out rapidly, to whatever degree of accuracy is required,[13] the negative eigenvalue theorem offers a significant improvement over variational methods, which have been limited in application to the determination of an upper bound for the lowest eigenvalue or, correspondingly, a lower bound for the longest relaxation time (time lag) for the system to approach steady state.[12]

Figures 6 and 7 show cumulative distributions for the eigenvalues of **H** obtained through repeated applications of the negative eigenvalue theorem as described in the Appendix. Figure 6 (distribution a) shows a clear separation of eigenvalues of **H** for the 2D network, implying a corresponding separation in time scales for relaxation of the time-dependent cluster population given by Eq. (2.21). Here the number of small eigenvalues, 25, is equal to $n2$ max, suggesting that the long time behavior in Eq. (2.21) is controlled by relaxation in the acid coordinate direction. Further evidence for this interpretation can be obtained by setting $\beta_2=0$ to obtain distribution b of the figure. Here the total number of eigenvalues is greatly reduced since only pure water clusters, corresponding to the lower row of nodes in Fig. 2, remain connected to the monomer source. In this case relaxation is to the equilibrium water cluster distribution, since the nucleation rate for pure water is zero at 50% RH. Comparison of the a and b cumulative eigenvalue distributions suggests that the large eigenvalues of the full 2D network (distribution a), which govern the short time behavior in Eq.

Downloaded¬14¬Mar¬2005¬to¬130.199.3.2.¬Redistribution¬subject¬to¬AIP¬license¬or¬copyright,¬see¬http://jcp.aip.org/jcp/copyright.jsp

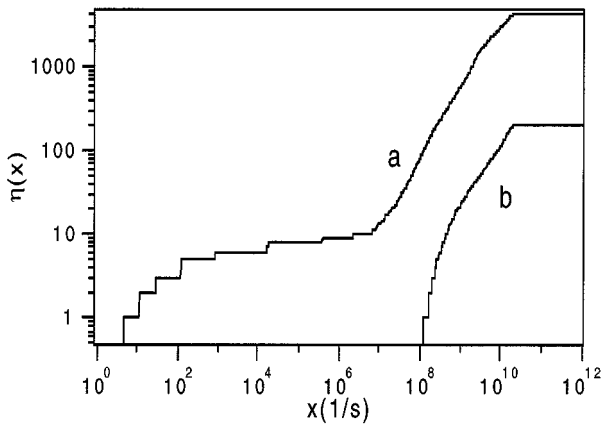

FIG. 7. Cumulative eigenvalue distribution for water RH=200% and acid activity=$1.2e-06$ (curve a). Plots show $\eta(x)$ for 1000 point sampling of Fig. 6. Units of x are s^{-1}. Curve b gives the cumulative eigenvalue distribution for pure water at 200% RH, corresponding to relaxation of the water cluster ($j=0$) population.

(2.21), result from rapid relaxation in the water coordinate direction. This wide separation of time scales underlies the quantitative agreement found between the SHR model and the present 2D calculations seen at 50% RH in Table II. Indeed the postulate of time scale separation is fundamental to the SHR model (Sec. IV C). Figure 7 shows similar results for the 200% RH calculation. Here the number of small eigenvalues is less than $n2$ max and there is somewhat less time scale separation.

The negative eigenvalue theorem, through its ability to localize the eigenvalues of **H**, can also be used for accurate determination of the corresponding eigenvectors through the technique of inverse iteration.[13] Although eigenvector calculations are beyond the scope of the present study, it should be noted that inverse iteration is expected to be especially well suited to the determination of long time behavior in Eq. (2.21) due to the wide separation of the smallest eigenvalues seen in Figs. 6 and 7.

The smallest eigenvalues are located at 11 s^{-1} for 50% RH (Fig. 6) and 4.8 s^{-1} for 200% RH (Fig. 7)—as indicated by the smallest values of x for which $\eta(x)=1$. The reciprocals of these values give the corresponding nucleation time lags. Interestingly, the time lags estimated in Ref. 12 using the variation method are of the same order of magnitude as those obtained here, despite use of the full 2D kinetics model and a different equilibrium vapor pressure for sulfuric acid in the present calculations.

C. Comparison with the Shugard–Heist–Reiss model

In the preceding sections, the general 2D kinetics model of Sec. II was applied to a specific binary system, sulfuric acid–water, with strong asymmetry in the physical properties of its two components. This asymmetry, while not required in the general model can, when justified, be used to derive a convenient, closed form, expression for the steady-state nucleation rate.[10] The result is similar in structure to the Becker–Doring rate formula,[4] but with double summation over the two-component indices (i and j) characterizing the binary cluster state:

$$J=\left(\frac{f_1}{n_1}-\frac{f_s}{n_s}\right)\left\{\sum_j\left[\sum_i \beta_2 s(i,j)n(i,j)\right]^{-1}\right\}^{-1}. \quad (4.1)$$

Equation (4.1) contains the same parameters that occur in the elements of **K** (Table I) and is compared with the present 2D model predictions for the steady-state nucleation rate in Table II. Equation (4.1) is identical to Eq. (18) of Ref. 10 for potentials $f_1/n_1=1$, and $f_s/n_s=0$ along the Szilard boundary for sufficiently large j.

The results of Secs. IV A and IV B suggest a quantitative range of validity to the physical assumptions behind Eq. (4.1) that could not have been demonstrated prior to carrying out the full 2D rate calculations. This success warrants further investigation. Returning to the resistor network analogy introduced in Sec. II, the term in curly brackets in Eq. (4.1) approximates the overall resistance of the network as

$$R=\sum_j\left[\sum_i \beta_2 s(i,j)n(i,j)\right]^{-1}. \quad (4.2)$$

With the definitions

$$\frac{1}{R_j}=\sum_i \beta_2 s(i,j)n(i,j) \quad (4.3)$$

and

$$\frac{1}{R_{i,j}}=\beta_2 s(i,j)n(i,j) \quad (4.4)$$

the double summation is equivalent to a series/parallel resistor model of the network. This is shown as follows. Referring to Fig. 2, the resistance $R_{i,j}$ is assigned to the network segment emanating in the vertical direction from node i,j. These are summed in parallel over index i in Eq. (4.3) to obtain R_j. The latter is the aggregate resistance from row j to row $j+1$ in Fig. 2. The R_j are, in turn, summed in series in Eq. (4.2) to obtain the overall network resistance R. The approximation requires that all nodes along a row (constant j) be at the same potential (f/n), which in general will be a function of j. A necessary, but not sufficient, requirement for this to hold is that the inequality, Eq. (3.3), be satisfied. Only then will the horizontal resistance links, connecting nodes i,j and $i+1,j$ in Fig. 2 and defined with β_1 replacing β_2 in Eq. (4.4), be small enough, relative to the vertical resistance links, for the equipotential condition to hold. (This same inequality was used in Sec. III as a convenient way to handle hydrates in sulfuric acid–water mixtures, but is otherwise not required in a 2D kinetics model.) The equipotential condition, implying zero net current along network rows of constant j, is equivalent to the assumption of local equilibrium with respect to the addition of water molecules used in the derivation of Eq. (4.1) in Ref. 10. Under conditions of local equilibrium, the summation over the water index i [Eq. (4.1)] provides an effective accounting for the width of the current distribution passing through the saddle.

Downloaded¬14¬Mar¬2005¬to¬130.199.3.2.¬Redistribution¬subject¬to¬AIP¬license¬or¬copyright,¬see¬http://jcp.aip.org/jcp/copyright.jsp

As noted above, the inequality, Eq. (3.3), is not sufficient for Eq. (4.1) to hold. Since the Szilard boundary condition sets $f/n=0$ for sufficiently large i (Fig. 2), the potential will, in fact, not be constant along a row of network nodes and the assumption of local equilibrium cannot strictly be met. Failure of the local equilibrium assumption is most pronounced at high water RH, where the nucleation flux is found to be predominantly in the i-coordinate direction for sufficiently large j. Under these conditions, as seen in Table II, Eq. (4.1) underestimates the nucleation rate. At low water RH, on the other hand, the vertical Szilard boundary (Fig. 2) lies in an inaccessible region of cluster space due to the high free-energy barrier (Fig. 3); a feature that permits local equilibrium independent of the f/n value maintained along that segment of the Szilard boundary. Then, as found above, Eq. (4.1) is an excellent approximation to the full 2D kinetics result. Further insight into the local equilibrium assumption, based on the required separation in the time scales for relaxation in the i- and j-coordinate directions,[10] can be found in the cumulative eigenvalue distributions.

V. DISCUSSION

Classical nucleation theory has been extended to obtain a consistent, fully two-dimensional treatment of nucleation kinetics in binary vapor mixtures. The extended, 2D model includes a generalization of the Szilard boundary condition, which now applies to a one-dimensional boundary set of clusters all of which exceed the thermodynamically defined critical cluster size. The nucleation rate consists of contributions from all possible paths throughout the cluster network and is evaluated as a sum of contributions over all currents reaching the Szilard boundary. The 2D kinetics model provides a quantitative method for testing the reduced dimensionality assumption invoked in conventional 1D models of binary nucleation that prescribe a fixed, usually thermodynamically derived, nucleation path. The model has been presented here for nearest-neighbor cluster transformations ($\Delta i=\pm 1$, $\Delta j=\pm 1$), but is easily adapted to the more general case.

For time-dependent studies, a new method, based on the negative eigenvalue theorem, was developed to obtain the distribution of relaxation times governing the approach to steady state. Specifically, the relaxation times were obtained as reciprocals of the eigenvalues of the Hermitian rate matrix **H**, which was shown in Sec. II B to provide a complete solution for the time-dependent current distribution and nucleation rate. The new method affords a highly efficient means of eigenvalue localization, that can be used for single-component as well as for binary nucleation studies and is, therefore, a significant improvement over variational methods, which have been limited to the determination of an upper bound on the lowest eigenvalue, corresponding to a lower bound on the time lag for approach to steady state.

Calculations were presented for the steady-state current distribution and relaxation time distribution for binary nucleation in sulfuric acid–water mixtures. Here the model was applied to a system whose individual components have very different physical properties, including hydrate clustering of the minority (acid) component in the vapor phase. Comparisons for the steady-state nucleation rate suggest a quantitative range of validity to the model of Shugard *et al.*[10] that could not have been demonstrated prior to a full 2D analysis of flux contributions to the nucleation rate. Side-by-side comparisons with the flux distributions and relaxation times obtained by the full 2D kinetics model, and from an analysis based on the resistor network model, indicate that the closed-form rate expression of Ref. 10 [Eq. (4.1)] can be used with confidence under conditions important for atmospheric new particle formation.

At high supersaturation (300% RH), in the realm of diffusion cloud chamber operation, the nucleation flux was found to bypass the saddle point, thereby violating a key assumption made in the conventional 1D saddle path models. Under these conditions, the full 2D kinetics model is required to obtain accurate assessments of the flux distribution and nucleation rate, which are shaped by a combination of kinetic and thermodynamic forcing.

ACKNOWLEDGMENTS

This research was supported in part by NASA through interagency agreement number W-18,429 as part of its interdisciplinary research program on tropospheric aerosols and was performed under the auspices of the United States Department of Energy, under Contract No. DE-AC02-76CH00016. The author gratefully acknowledges Dr. Stephen E. Schwartz of BNL for many valuable discussions and Dr. Francis Canning of the Rockwell International Science Center for advice on handling sparse matrix systems.

APPENDIX: APPLICATION OF THE NEGATIVE EIGENVALUE THEOREM

Presented below is a description of the negative eigenvalue theorem, followed by a convenient reformulation of the algorithm recommended for banded symmetric matrices stored in compressed form. Proof of the theorem and its use in the determination of eigenvectors through inverse iteration can be found in Ref. 13.

The negative eigenvalue theorem provides an efficient method for computing the eigenvalues of a real symmetric matrix. The particular form of the theorem that we will apply rest upon partitioning **H** into four submatrices: $\mathbf{A_1}$, $\mathbf{A_2}$, $\mathbf{B_1}$, and $\mathbf{B_1^T}$, with $\mathbf{A_1}$ of order unity (i.e., scalar):

$$\mathbf{H}=\begin{bmatrix}\mathbf{A_1} & \mathbf{B_1}\\ \mathbf{B_1^T} & \mathbf{A_2}\end{bmatrix}, \tag{A1}$$

where

$$\mathbf{A_1}=\mathbf{a_{11}},$$

$$\mathbf{B_1}=(\mathbf{a_{12}},\mathbf{a_{13}},\ldots,\mathbf{a_{1n}}), \tag{A2}$$

$$\mathbf{A_2}=\begin{bmatrix}\mathbf{a_{22}} & \mathbf{a_{23}} & . & . & \mathbf{a_{2n}}\\ \mathbf{a_{32}} & \mathbf{a_{33}} & . & . & \mathbf{a_{3n}}\\ . & . & & & .\\ . & . & & & .\\ \mathbf{a_{n2}} & . & . & . & \mathbf{a_{nn}}\end{bmatrix},$$

and $\mathbf{B_1^T}$ is the transpose of $\mathbf{B_1}$. Next consider the matrix $\mathbf{M_1}(x)=\mathbf{H}-x\mathbf{I}$ where x is a positive real number and **I** is the

Downloaded¬14¬Mar¬2005¬to¬130.199.3.2.¬Redistribution¬subject¬to¬AIP¬license¬or¬copyright,¬see¬http://jcp.aip.org/jcp/copyright.jsp

identity matrix, also of order n. Now $\mathbf{H}$ will have precisely $\eta\{\mathbf{M_1}(x)\}$ of its eigenvalues less than x, where $\eta\{\mathbf{M_1}(x)\}$ is defined as the number of negative eigenvalues of $\mathbf{M_1}(x)$. By choosing different values for x, and evaluating $\eta\{\mathbf{M_1}(x)\}$ for each, the distribution, and/or localization, of the eigenvalues of $\mathbf{H}$ is determined. The negative eigenvalue theorem provides the means to determine $\eta\{\mathbf{M_1}(x)\}$.

Dean[13] introduces the following notation:

$$\mathbf{X_1}=\mathbf{A_1}-\mathbf{xI_1},$$
$$\mathbf{Z_1}=\mathbf{A_2}-\mathbf{xI_2}, \tag{A3}$$
$$\mathbf{Y_1}=\mathbf{B_1},$$

where the matrices on the right-hand side are as defined in Eq. (A2). In this new notation the partitioning of $\mathbf{H}-x\mathbf{I}$ takes the form

$$\mathbf{M_1}(\mathbf{x})=\begin{bmatrix}\mathbf{X_1} & \mathbf{Y_1}\\ \mathbf{Y_1^T} & \mathbf{Z_1}\end{bmatrix} \tag{A4}$$

and the negative eigenvalue theorem gives the result

$$\eta[\mathbf{M_1}(\mathbf{x})]=\eta[\mathbf{X_1}]+\eta[\mathbf{Z_1}-\mathbf{Y_1^T}\mathbf{X_1^{-1}}\mathbf{Y_1}]. \tag{A5}$$

Since $\mathbf{X_1}$ is a scalar, the first term on the right-hand side of Eq. (A5) is simply determined from the sign of $\mathbf{X_1}$. It is equal to 0 (1) when the sign of $a_{11}-x$ is positive (negative). Thus $\eta\{\mathbf{M_1}(x)\}$ equals the sum of this result and the number of negative eigenvalues of the square matrix $\mathbf{Z_1}-\mathbf{Y_1^T}\mathbf{X_1^{-1}}\mathbf{Y_1}$ of order $n-1$. The entire process is now repeated for the symmetric square matrix of order $n-1$ by defining

$$\mathbf{M_2}(\mathbf{x})=\mathbf{Z_1}-\mathbf{Y_1^T}\mathbf{X_1^{-1}}\mathbf{Y_1}=\begin{bmatrix}\mathbf{X_2} & \mathbf{Y_2}\\ \mathbf{Y_2^T} & \mathbf{Z_2}\end{bmatrix} \tag{A6}$$

and a second application of the theorem is given in analogy to Eq. (A5):

$$\eta[\mathbf{M_2}(\mathbf{x})]=\eta[\mathbf{X_2}]+\eta[\mathbf{Z_2}-\mathbf{Y_2^T}\mathbf{X_2^{-1}}\mathbf{Y_2}]. \tag{A7}$$

Continuation of the process gives

$$\eta[\mathbf{M_1}(\mathbf{x})]=\sum_{\mathbf{i=1}}^{\mathbf{n}}\eta[\mathbf{X_i}] \tag{A8}$$

for the number of negative eigenvalues of $\mathbf{M_1}(x)$ or, equivalently, for the number of eigenvalues of $\mathbf{H}$ less than x, which is the desired result.

Storage limitations require that $\mathbf{H}$ be handled in compressed form. Figure 8 shows the matrix $\mathbf{M_1}(x)$ in the compressed format $\mathbf{M_R}(x)$ used in the subroutines for matrix inversion.[17] This format actually turns out to be advantageous for coding the negative eigenvalue algorithm. The full symmetric matrix bandwidth is $2h-1$. Comparison of Eqs. (A2) and Fig. 8 shows that elements of the compressed and uncompressed matrices are related as

$$[\mathbf{M_1}(\mathbf{x})]_{\mathbf{i,j}}=[\mathbf{M_R}(\mathbf{x})]_{\mathbf{i,j-i+1}}, \tag{A9}$$

where the subscript R labels the compressed form. The quantities

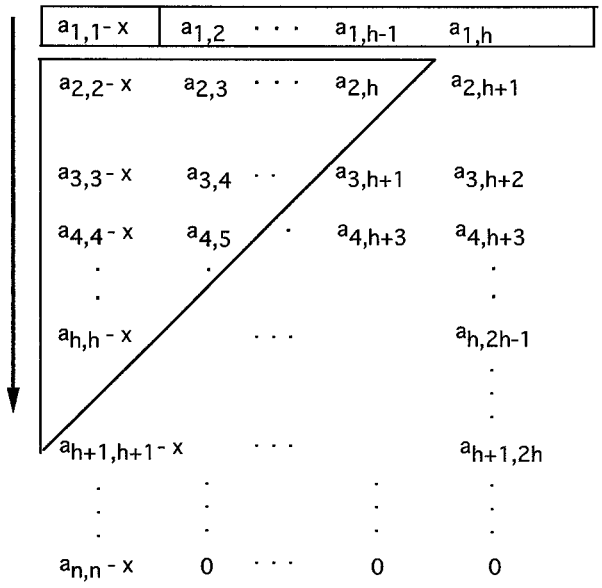

FIG. 8. Application of the negative eigenvalue theorem to banded matrices in compressed form.

$$\mathbf{X_1}=[\mathbf{M_R}(\mathbf{x})]_{\mathbf{1,1}},$$
$$\mathbf{Y_1(j)}=[\mathbf{M_R}(\mathbf{x})]_{\mathbf{1,j+1}} \tag{A10}$$

define the header row of the compressed matrix. The triangular region that includes elements from the $h-1$ rows immediately below the header row is the work space, namely that region of $\mathbf{Z_1}$ over which the subtraction of the elements in the product $\mathbf{Y_1^T}\mathbf{X_1^{-1}}\mathbf{Y_1}$ occurs. Specifically,

$$[\mathbf{M_R}(\mathbf{x})]_{\mathbf{i+1,j-i+1}}=[\mathbf{M_R}(\mathbf{x})]_{\mathbf{i+1,j-i+1}}-\mathbf{X_1^{-1}}\mathbf{Y_1(i)}\mathbf{Y_1(j)} \tag{A11}$$

for i, $j=1$ through $h-1$ with $j\geq i$.

Header and work space templates are then shifted down one row in the direction of the arrow and the process repeated until n signs of the first elements each header row $\eta[\mathbf{X_i}]$ have been accumulated for evaluation of Eq. (A8). At step L:

$$\mathbf{X_L}=[\mathbf{M_R}(\mathbf{x})]_{\mathbf{L,1}},$$
$$\mathbf{Y_L(j)}=[\mathbf{M_R}(\mathbf{x})]_{\mathbf{L,j+1}}, \tag{A12}$$
$$[\mathbf{M_R}(\mathbf{x})]_{\mathbf{i+L,j-i+1}}=[\mathbf{M_R}(\mathbf{x})]_{\mathbf{i+L,j-i+1}}-\mathbf{X_L^{-1}}\mathbf{Y_L(i)}\mathbf{Y_L(j)}. \tag{A13}$$

Additional rows of zeros may be appended to the array of Fig. 8 to prevent the triangular work space from entering, in the final steps of the calculation, an undefined region.

[1] W. A. Hoppel, J. W. Fitzgerald, G. M. Frick, and R. E. Larson, J. Geophys. Res. **95**, 3659 (1990).
[2] F. Raes, J. Geophys. Res. (in press).
[3] G. A. Herbert, R. C. Schnell, H. A. Bridgman, B. A. Bodhaine, S. J. Oltmans, and G. E. Shaw, J. Atmos. Chem. **9**, 17 (1989).
[4] F. F. Abraham, *Homogeneous Nucleation Theory* (Academic, New York, 1974), p. 85.

Downloaded 14 Mar 2005 to 130.199.3.2. Redistribution subject to AIP license or copyright, see http://jcp.aip.org/jcp/copyright.jsp

[5] D. Stauffer, J. Aerosol. Sci. **7**, 319 (1976).
[6] H. M. Ellerby, C. L. Weakliem, and H. Reiss, J. Chem. Phys. **95**, 9209 (1991).
[7] C. L. Weakliem and H. Reiss, J. Chem. Phys. **101**, 2398 (1994).
[8] W. J. Shugard and H. Reiss, J. Chem. Phys. **65**, 2827 (1976).
[9] A. Jaecker-Voirol and P. Mirabel, J. Phys. Chem. **92**, 3518 (1988).
[10] W. J. Shugard, R. H. Heist, and H. Reiss, J. Chem. Phys. **61**, 5298 (1974).
[11] R. H. Heist and H. Reiss, J. Chem. Phys. **61**, 573 (1974).
[12] F. J. Schelling and H. Reiss, J. Chem. Phys. **74**, 3527 (1981).
[13] P. Dean, Rev. Mod. Phys. **44**, 127 (1972).
[14] H. Vehkamaki, P. Paatero, M. Kulmala, and A. Laaksonen (preprint).
[15] K. Chu and R. A. Morrison, in *Environmental and Climatic Impact of Coal Utilization*, edited by J. J. Singh and A. Deepak (Academic, New York, 1980), p. 293.
[16] G. P. Ayers, R. W. Gillet, and J. L. Gras, Geophys. Res. Lett. **7**, 433 (1980).
[17] W. H. Press, W. T. Vetterling, S. A. Teukolsky, and B. P. Flannery, *Numerical Recipes in Fortran* (Cambridge, New York, 1992), p. 42.

Downloaded¬14¬Mar¬2005¬to¬130.199.3.2.¬Redistribution¬subject¬to¬AIP¬license¬or¬copyright,¬see¬http://jcp.aip.org/jcp/copyright.jsp